

Crystal structure and spin-trimer magnetism of $\text{Rb}_{2.3}(\text{H}_2\text{O})_{0.8}\text{Mn}_3[\text{B}_4\text{P}_6\text{O}_{24}(\text{O},\text{OH})_2]$

**Olga V. Yakubovich, Larisa V. Shvanskaya, Galina V. Kiriukhina,
Anatoly S. Volkov, Olga V. Dimitrova, Evgeny A. Ovchenkov,
Alexander A. Tsirlin, Alexander A. Shakin, Olga S. Volkova,
Alexander N. Vasiliev**

Angaben zur Veröffentlichung / Publication details:

Yakubovich, Olga V., Larisa V. Shvanskaya, Galina V. Kiriukhina, Anatoly S. Volkov, Olga V. Dimitrova, Evgeny A. Ovchenkov, Alexander A. Tsirlin, Alexander A. Shakin, Olga S. Volkova, and Alexander N. Vasiliev. 2017. "Crystal structure and spin-trimer magnetism of $\text{Rb}_{2.3}(\text{H}_2\text{O})_{0.8}\text{Mn}_3[\text{B}_4\text{P}_6\text{O}_{24}(\text{O},\text{OH})_2]$." Dalton Transactions 46 (9): 2957–65. <https://doi.org/10.1039/c6dt04241d>.

Cite this: *Dalton Trans.*, 2017, **46**,
2957

Crystal structure and spin-trimer magnetism of $\text{Rb}_{2.3}(\text{H}_2\text{O})_{0.8}\text{Mn}_3[\text{B}_4\text{P}_6\text{O}_{24}(\text{O},\text{OH})_2]^\dagger$

Olga V. Yakubovich,^a Larisa V. Shvanskaya,^{a,b} Galina V. Kiriukhina,^a Anatoly S. Volkov,^a Olga V. Dimitrova,^a Evgeny A. Ovchenkov,^a Alexander A. Tsirlin,^{c,d} Alexander A. Shakin,^b Olga S. Volkova^{a,b,e} and Alexander N. Vasiliev^{*a,b,e}

The novel borophosphate $\text{Rb}_{2.3}(\text{H}_2\text{O})_{0.8}\text{Mn}_3[\text{B}_4\text{P}_6\text{O}_{24}(\text{O},\text{OH})_2]$ was prepared under hydrothermal conditions at 553 K. Its crystal structure was determined using single-crystal X-ray diffraction data obtained from a non-merohedral twin and refined against F^2 to $R = 0.057$. The compound crystallizes in the orthorhombic space group $Pbcn$, with unit-cell parameters $a = 20.076(2)$ Å, $b = 9.151(1)$ Å, $c = 12.257(1)$ Å, $V = 2251.8(2)$ Å³, and $Z = 4$. The title compound is the first example of a borophosphate with manganese ions adopting both octahedral and tetrahedral coordinations. Its unique crystal structure is formed by borophosphate slabs and chains of Mn^{2+} -centered polyhedra sharing edges and vertices. These 2D and 1D fragments interconnect into a framework with open channels that accommodate Rb^+ cations and water molecules. Topological relationships between borophosphates built from three-membered rings of two borate and one phosphate tetrahedra sharing oxygen vertices, amended by additional PO_4 and HPO_4 tetrahedra, are discussed. The temperature dependence of the magnetic susceptibility of $\text{Rb}_{2.3}(\text{H}_2\text{O})_{0.8}\text{Mn}_3[\text{B}_4\text{P}_6\text{O}_{24}(\text{O},\text{OH})_2]$ reveals predominant antiferromagnetic exchange interactions and the high-temperature effective magnetic moment corresponding to the high-spin $S = 5/2$ state of Mn^{2+} ions. At 12.5 K, a magnetic transition is evidenced by ac-susceptibility and specific heat measurements. A spin-trimer model with the leading exchange interaction $J \sim 3.2$ K is derived from density-functional band-structure calculations and accounts for all experimental observations.

Received 7th November 2016,
Accepted 31st January 2017

DOI: 10.1039/c6dt04241d

rsc.li/dalton

Introduction

The chemical class of borophosphates comprises compounds with crystal structures built by PO_4 and BO_4/BO_3 oxocomplexes sharing oxygen vertices. Similar to silicates, complex borophosphate anions may be zero-, one-, two- and three-dimensional oligomer units forming chains, layers or frameworks.¹ Intensive exploration of borophosphates in the last two decades is due to their fascinating structural chemistry and numerous technological applications.^{2,3} Lithium iron borophosphate, $\text{Li}_{0.8}\text{Fe}(\text{H}_2\text{O})_2[\text{BP}_2\text{O}_8]\cdot\text{H}_2\text{O}$, reveals electrochemical

activity as a cathode material for Li- and Na-ion batteries,⁴ while $\text{Sn}_x(\text{Ca}_{0.05}\text{B}_{0.975}\text{P}_{0.975}\text{O}_{3.95})_{1-x}/\text{C}$ composites can be used as anode materials for Li-ion batteries.⁵

Borophosphates may also have interesting connections to abiogenesis. According to ref. 6, some prebiological episodes could occur in environments with borophosphates, which arguably took part in special reactions in the form of hydrogels. Their derived chiral minerals served as drivers for prebiotic processes, thus providing conditions for the appearance of protocells.

Borophosphates with open microporous structures often comprise metal oxocomplexes and, therefore, not only exhibit adsorption, catalytic, and ion-conductive properties typical of zeolite-like compounds, but also demonstrate promising physical characteristics which depend on the nature of constituent metal atoms. The incorporation of transition metals into the borophosphate framework often leads to interesting features of forming phases.^{7,8}

Particularly, borophosphates with Mn^{2+} -cations are of special interest not only with respect to catalysis applications, but also as potential materials with luminescence and magnetic properties. For example, $(\text{NH}_4)_7\text{Mn}_4(\text{H}_2\text{O})[\text{B}_2\text{P}_4\text{O}_{15}(\text{OH})_2]_2(\text{H}_2\text{PO}_4)(\text{HPO}_4)$ crystals with 16 ring pore

^aM.V. Lomonosov Moscow State University, Moscow 119991, Russia.

E-mail: vasil@mig.phys.msu.ru

^bNational University of Science and Technology "MISIS", 119049 Moscow, Russia^cExperimental Physics VI, Center for Electronic Correlations and Magnetism,

Institute of Physics, University of Augsburg, D-86135 Augsburg, Germany

^dNational Institute of Chemical Physics and Biophysics, 12618 Tallinn, Estonia^eInstitute of Physics and Technology, Ural Federal University, 620002 Ekaterinburg, Russia[†]Electronic supplementary information (ESI) available: Crystallographic information for $\text{Rb}_{2.3}(\text{H}_2\text{O})_{0.8}\text{Mn}_3[\text{B}_4\text{P}_6\text{O}_{24}(\text{O},\text{OH})_2]$, the results of bond valence calculation and magnetic measurement data (PDF) and X-ray crystallographic data in CIF format (CIF). See DOI: 10.1039/c6dt04241d

openings show antiferromagnetic interactions between Mn^{2+} ions.⁹ $\text{KMnBP}_2\text{O}_7(\text{OH})_2$ demonstrates long-range antiferromagnetic ordering and exhibits bright orange luminescence at room temperature.¹⁰ Another Mn^{2+} borophosphate, $(\text{NH}_4)_6[\text{Mn}_3\text{B}_6\text{P}_9\text{O}_{36}(\text{OH})_3]\cdot 4\text{H}_2\text{O}$, reveals canted antiferromagnetic order at low temperatures.¹¹

In our search for functional crystals with transition metals and mixed anionic arrangement, a novel water-bearing rubidium manganese borophosphate was obtained under hydrothermal conditions. The new compound is characterized by a unique combination of six-fold and four-fold-coordinated Mn^{2+} cations, not mentioned before to our knowledge. We present here its crystal structure and magnetic properties in comparison with related compounds featuring borophosphate slabs of similar topology.

Experimental section

Synthesis and structure determination

Colourless transparent needle crystals of the new phase with a maximum length of 200 μm (Fig. 1) were prepared hydrothermally in the $\text{Rb}_2\text{CO}_3\text{-MnCl}_2\text{-H}_3\text{PO}_4\text{-B}_2\text{O}_3$ system. A mixture of these components at the 1 : 2 : 2 : 4 weight ratio was placed into a 4 ml stainless steel bomb with distilled water filling 80% of the volume. The experiment was con-

ducted at a temperature of 553 K and a pressure of 70 bar over a period of 18 days followed by cooling of the furnace to room temperature. The reaction products in the form of druses of needle crystals were washed with water and dried. Their phase purity was confirmed by the agreement between the experimental powder X-ray diffraction pattern and the simulated diagram based on the single-crystal structural data.

A suitable single crystal of the title compound was analyzed with a scanning electron microscope (SEM)† JEOL SEM (JSM-6480LV) equipped with an INCA Energy-350 energy dispersive (EDS) detector and an INCAWave-500 four-crystal wavelength dispersive spectrometer (WDS). The measurements were made at 20 kV and 7 nA, and the sample was stable under these conditions. X-ray spectral analysis provided a semi quantitative result with the Rb : Mn : P : B : O ratio close to 1 : 1.5 : 3 : 2 : 15, which is consistent with the results of our X-ray diffraction structural study.

The single crystal X-ray diffraction data were collected at ambient temperature by using graphite-monochromated $\text{Mo-K}\alpha$ radiation with an Xcalibur-S area detector diffractometer. The intensities were corrected for Lorentz and polarization effects, and a numerical absorption correction based on Gaussian integration over a multifaceted crystal model was applied. An analysis of the experimental set of X-ray reflections with CrysAlisPro¹² has shown that the studied crystal was a non-merohedral twin with a twinning angle of about 8.5°. The reflections from different components of the sample were separated in the new set. 12% of reflections with partial overlap, for which individual contributions could not be revealed, were removed. All calculations were performed in the WinGX32 software package.¹³ Atomic scattering factors and anomalous dispersion corrections were taken from the International Tables for Crystallography.¹⁴

The crystal structure was solved *via* direct methods in the space group $Pbcn$ and refined against the F^2 data with SHELX programs.¹⁵ The final refinement was performed on the basis of all experimental intensities marked for each component in the HKLF5 reflection file, to the R factor of 0.057 (for 1891 unique reflections with $I > 2\sigma(I)$) with anisotropic displacement parameters for all non-hydrogen atoms. The positions of one independent H atom forming the hydroxyl group were obtained by difference-Fourier techniques and refined in an isotropic approximation. The O–H bond length was fixed by hard restraints to an empirical value of 0.85 Å in order to obtain comparable H-bond geometry not affected by arbitrary scatter of the refined O–H distance. The crystallographic characteristics of the new phase, the experimental conditions of the data collection, and the final results of the structure refinement are shown in Table 1. Table S1† presents the atomic positions and equivalent isotropic displacement para-

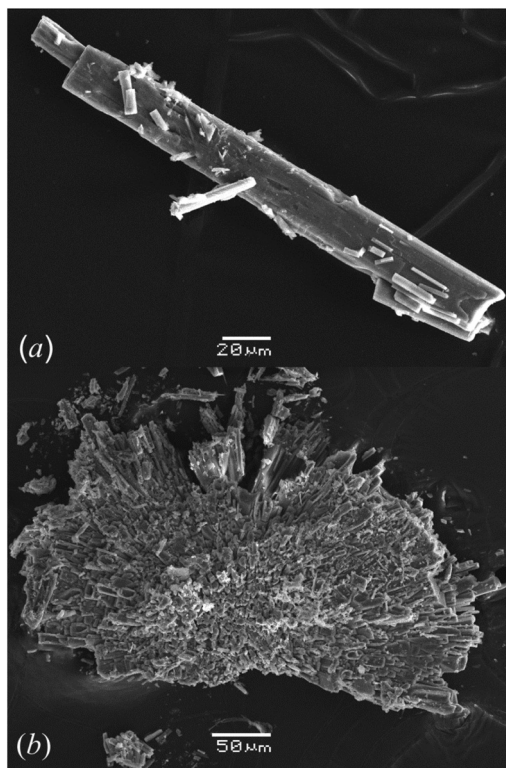


Fig. 1 SEM images of the title phase, showing the druse of growing crystals (a) and the crystal morphology (b).

† The analysis was performed at the Laboratory of Local Methods for Studying Materials, Department of Petrology, Faculty of Geology, M.V. Lomonosov Moscow State University.



Table 1 Crystal information and details of the X-ray data collection and refinement

Crystal data	
Chemical formula,	Rb _{2.26} (H ₂ O) _{0.76} Mn ₃ {B ₄ P ₆ O ₂₄ [(OH) _{1.74} O _{0.26}] ₂ }
<i>M</i> (g mol ⁻¹)	1017.1
Crystal system,	Orthorhombic, <i>Pbcn</i> (no. 60)
space group	
<i>a</i> , <i>b</i> , <i>c</i> (Å)	20.0755(12), 9.1512(8), 12.2568(7)
<i>V</i> (Å ³), <i>Z</i>	2251.8(3), 4
<i>D</i> _c (g cm ⁻³)	3.000
Crystal size (mm)	0.110 × 0.040 × 0.020
Crystal colour	Colourless
Absorption coeff.	7.07
<i>μ</i> (mm ⁻¹)	
Data collection	
Diffractometer	Xcalibur-S, CCD
Radiation	Mo-K _α (λ = 0.71073 Å), graphite monochromator
Temperature (K)	298(2)
Scanning mode	<i>ω</i>
Measuring range	θ _{max} = 27.493°
Reflections (total)	6312
<i>h</i> , <i>k</i> , <i>l</i> range	-25 ≤ <i>h</i> ≤ 26, -11 ≤ <i>k</i> ≤ 7, -15 ≤ <i>l</i> ≤ 15
Refinement	
Reflections observed (<i>I</i> > 2σ(<i>I</i>))	1891
Number of parameters used in the refinement	178
Absorption correction,	Numerical, 0.574, 0.847
<i>T</i> _{max} , <i>T</i> _{min}	
Parameter of twinning (BASF)	0.343(1)
Residuals	
<i>R</i> (observed reflections)	0.057
<i>wR</i> ₂ (all reflections)	0.086
Δρ (max/min) (e Å ⁻³)	1.60, -1.24

meters. Characteristic interatomic distances are given in Table 2. A bond-valence calculation (Table S2†) has been performed using the algorithm and parameters listed in ref. 16 and 17; its results are consistent with the assumed oxidation state of +2 for Mn and clearly confirm the assignment of the OH and H₂O groups. According to our structural model, O10 corresponds to a mixed (O, OH) populated position in the 0.13 : 0.87 ratio. The synthesized phase is described by the following chemical formula: Rb_{2.26}(H₂O)_{0.76}Mn₃{B₄P₆O₂₄[(OH)_{1.74}O_{0.26}]₂}. Idealized formula can be written as Rb_{2.3}(H₂O)_{0.8}Mn₃[B₄P₆O₂₄(O,OH)₂].

Measurements of thermodynamic properties

The magnetic properties of Rb_{2.3}(H₂O)_{0.8}Mn₃[B₄P₆O₂₄(O,OH)₂] were investigated in the temperature range 2–300 K using both ac- and dc-magnetic susceptibility options of the “Quantum Design” Physical Properties Measurements System PPMS-9T. The magnetization of the title compound was measured up to 9 T in a static magnetic field and up to 30 T in a pulsed magnetic field at low temperatures. The specific heat of the pressed pellet of the sample was measured in the range 2–200 K by the relaxation method.

§ Additional materials to the crystal structure investigation are obtained from Fachinformationszentrum Karlsruhe, Germany, under specification of deposit No. CSD-431432 and authors' reference.

Table 2 Interatomic distances and hydrogen bond geometry, Å/°

P1 tetrahedron	P2 tetrahedron	P3 tetrahedron		
P1–O8 1.494(5)	P2–O6 1.510(6)	P3–O7 1.505(5)		
P1–O2 1.548(5)	P2–O3 1.522(7)	P3–O12 1.531(6)		
P1–O9 1.548(6)	P2–O4 1.547(6)	P3–O11 1.537(6)		
P1–O5 1.554(6)	P2–O1 1.551(5)	P3–O10 1.556(7)		
B1 tetrahedron	B2 tetrahedron	Mn1 octahedron		
B1–O13 1.444(11)	B2–O13 1.445(11)	Mn1–O6 2.117(4)		
B1–O9 1.476(11)	B2–O2 1.463(10)	Mn1–O12 2.156(5)		
B1–O5 1.480(12)	B2–O13 1.485(11)	Mn1–O8 2.157(6)		
B1–O1 1.491(11)	B2–O11 1.486(11)	Mn1–O3 2.189(4)		
		Mn1–O13 2.214(5)		
		Mn1–O12 2.259(6)		
Mn2 tetrahedron	Rb1 polyhedron	Rb2 polyhedron		
Mn2–O7 2.079(7) × 2	Rb1–O7 2.900(6)	Rb2–O14 2.45(2)		
Mn2–O3 2.107(5) × 2	Rb1–O9 2.906(5)	Rb2–O9 2.964(9)		
Rb3 polyhedron	Rb1–O2 2.931(5)	Rb2–O8 3.015(6)		
Rb3–O10 2.604(6) × 2	Rb1–O5 2.985(5)	Rb2–O7 3.120(10)		
Rb3–O6 2.929(9) × 2	Rb1–O8 2.995(5)	Rb2–O10 3.163(10)		
Rb3–O7 3.315(9) × 2	Rb1–O14 3.09(2)	Rb2–O2 3.256(9)		
	Rb1–O1 3.248(6)			
	Rb1–O3 3.278(7)			
D–H...A	D–H	H...A	D...A	D–H...A
O10–H1...O10	0.845(16)	1.87(7)	2.566(15)	139(10)

Results and discussion

Description of the crystal structure and discussion

The asymmetric unit of the structure (Fig. 2) includes three P sites and two B sites in a strongly distorted tetrahedral coordination. Three P1–O distances of about 1.55 Å and a short one of 1.494(5) Å characterize the P1O₄ polyhedron, while the P–O bond lengths in the P2O₄ and P3O₄ tetrahedra are in the range of 1.51–1.57 Å. In the BO₄ tetrahedron, the B–O distances vary from 1.44(1) to 1.49(1) Å (Table 2).

Manganese atoms show a strongly distorted octahedral coordination. The Mn–O distances are in the range of 2.117(4)–2.260(6) Å for Mn1; the Mn2 atoms are on the two-fold axis and surrounded by four O atoms forming tetrahedra with the Mn2–O bond lengths of 2.079(6) and 2.107(5) Å. Two

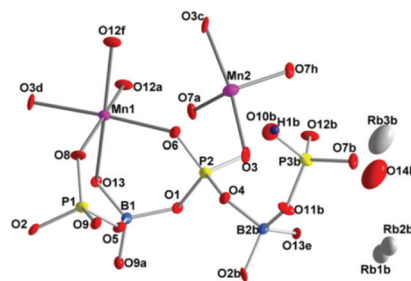


Fig. 2 Basic structural units with the atom labeling scheme. Displacement ellipsoids are presented at the 50% probability level. Symmetry codes: (a) $-x, \frac{1}{2} + y, z$; (b) $\frac{1}{2} - x, \frac{1}{2} - y, -\frac{1}{2} + z$; (c) $1 - x, y, \frac{1}{2} - z$; (d) $x, 1 - y, \frac{1}{2} + z$; (e) $x, 1 - y, -\frac{1}{2} + z$; (f) $\frac{1}{2} + x, \frac{1}{2} - y, 1 - z$; (h) $\frac{1}{2} + x, \frac{1}{2} + y, \frac{1}{2} - z$.



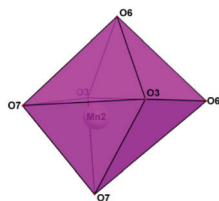


Fig. 3 Coordination polyhedron of Mn2 (CN 4 + 2).

additional O atoms are situated at longer distances of 2.940(6) Å (Fig. 3). The tetrahedral coordination is relatively uncommon for Mn²⁺, although it has been reported for the KMnPO₄ and RbMnPO₄ crystal structures.^{18,19} The patterns of the P-, B- and Mn-polyhedra distortion are consistent with the bond-valence calculation (Table S2†). Large low-charge Rb⁺ cations located in the voids of the framework and statistically distributed in three positions are surrounded by eight or six oxygen atoms. The Rb⁺ sites with 82% population feature six Rb1–O distances varying from 2.900(6) to 3.09(2) Å and two longer ones of 3.249(6) and 3.278(7) Å. According to our data, the hydroxyl groups substitute for one of the O atoms at the O10 vertices of the P3 tetrahedra. As a result, the [HPO₄] tetrahedra, which are adjacent in the [010] direction, become linked by means of an O10–H1...O10 hydrogen bond interaction (Table 2). With O...O distances of 2.566 Å, these bonds can be classified as strong.

Pairs of edge-sharing MnO₆ octahedra and MnO₄ tetrahedra alternate along the [001] direction and form corrugated chains parallel to the *c* axis of the orthorhombic unit cell (Fig. 4). A symmetrically independent fragment of the borophosphate anion presents a three-membered ring of two borate and one phosphate tetrahedra sharing oxygen vertices, amended by additional PO₄ and HPO₄ tetrahedra (Fig. 5a). These basic building units are reproduced by symmetry elements of the *Pbcn* space group and form anionic borophosphate slabs (Fig. 5b), which interchange along the *a* axis with the chains of Mn polyhedra (Fig. 6). The interconnection of the two-dimensional [B₄P₆O₂₄(O,OH)₂] sections and one-dimensional fragments of the Mn polyhedra results in thick

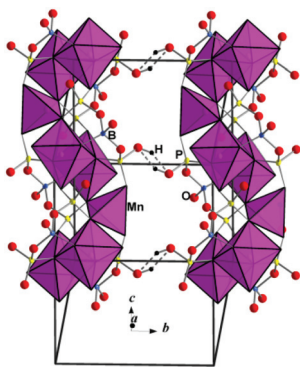


Fig. 4 Corrugated chains of edge-sharing MnO₆ octahedra and MnO₄ tetrahedra, associated with PO₄ and BO₄ tetrahedra.

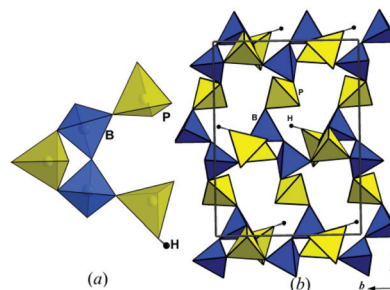


Fig. 5 The borophosphate anion built from PO₄ and BO₄ tetrahedra: a symmetrically independent fragment (a) and a two-dimensional slab (b).

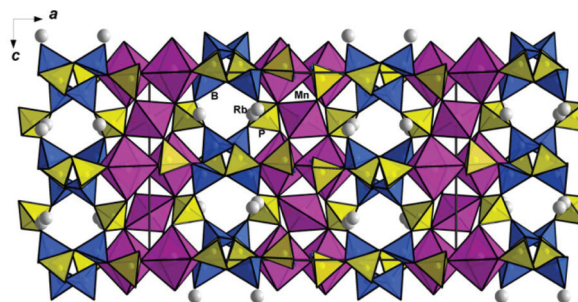


Fig. 6 The title crystal structure viewed along the *b* axis.

packages with the Mn₃[B₄P₆O₂₄(O,OH)₂] composition. The OH groups at the vertices of phosphate tetrahedra provide hydrogen bonding that has a strong influence on the structural arrangement. Thus, the bridging of the Mn₃[B₄P₆O₂₄(O,OH)₂] packages by hydroxyl groups in the *b* axis direction (Fig. 4) leads to a 3D framework with open channels running along [001]. These channels accommodate Rb⁺ cations and H₂O molecules (Fig. 7).

Topologically identical slabs built by phosphate and borate tetrahedra have been previously described in several other crystal structures, which are listed in Table 3. The first such cobalt borophosphate with organic molecules filling structural channels was reported by Sevov.²⁰ In the (C₂H₁₀N₂)Co[B₂P₃O₁₂(OH)] crystal structure, the borophosphate slabs with three- and nine-membered rings share oxygen vertices with

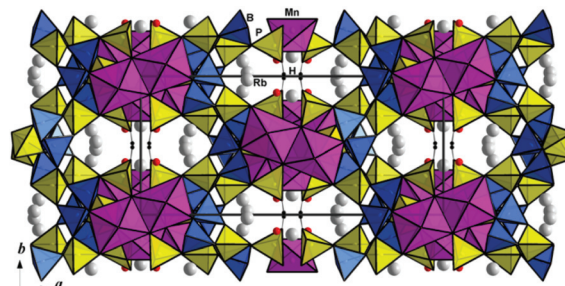


Fig. 7 The title crystal structure viewed along the *c* axis.



Table 3 Composition, crystal characteristics and selected distances for topologically related borophosphates

Formula, crystal structure details	Unit-cell parameters a, b, c , Å and V , Å ³	S.G., Z, ρ , g cm ⁻³	$\langle M-O \rangle$, Å	$\langle A-O \rangle$, Å	Ref.
(C ₂ H ₁₀ N ₂)Co[B ₂ P ₃ O ₁₂ (OH)] Borophosphate slabs and CoO ₆ octahedra form a 3D mixed anionic framework with organic molecules in channels	9.3501(5) 12.2426(9) 20.880(2) 2390.1(3)	<i>Pbca</i> 8 2.471	2.101 (M = Co ²⁺)	(A = C ₂ H ₁₀ N ₂)	20
(C ₂ H ₁₀ N ₂)Mg[B ₂ P ₃ O ₁₂ (OH)] Borophosphate slabs and MgO ₆ octahedra form a 3D mixed anionic framework with organic molecules in channels	9.3681(2) 12.2186(4) 20.8928(5) 2391.5(1)	<i>Pbca</i> 8 2.277	2.087 (M = Mg ²⁺)	(A = C ₂ H ₁₀ N ₂)	21
(C ₂ H ₁₀ N ₂)Cd[B ₂ P ₃ O ₁₂ (OH)] Borophosphate slabs and CdO ₆ octahedra form a 3D mixed anionic framework with organic molecules in channels	9.286(3) 12.459(3) 21.626(6) 2502(1)	<i>Pbca</i> 8 2.639	2.271 (M = Cd ²⁺)	(A = C ₂ H ₁₀ N ₂)	22
(C ₄ H ₁₆ N ₃)CdCl[B ₂ P ₃ O ₁₂ (OH)] Borophosphate slabs and CdO ₅ Cl octahedra form 2D mixed anionic packages with organic molecules between	9.470(2) 12.307(3) 27.311(6) 3183(1)	<i>Pbca</i> 8 2.411	2.318 ^b (M = Cd ²⁺)	(A = C ₄ H ₁₆ N ₃)	22
K ₂ (H ₂ O)Co[B ₂ P ₃ O ₁₂ (OH)] Borophosphate slabs and CoO ₆ octahedra form a 3D mixed anionic framework with K atoms and water molecules in channels	9.7255(7) 12.2075(8) 19.928(2) 2365.9(3)	<i>Pbca</i> 8 2.688	2.104 (M = Co ²⁺)	2.839 2.866 (A = K, H ₂ O)	23
K ₂ (H ₂ O)Ni[B ₂ P ₃ O ₁₂ (OH)] Borophosphate slabs and NiO ₆ octahedra form a 3D mixed anionic framework with K atoms and water molecules in channels	9.5543(2) 12.056(2) 19.814(4) 2282.3(8)	<i>Pbca</i> 8 2.681	2.100 (M = Ni ²⁺)	2.988 3.007 3.007 (A = K, H ₂ O)	23
RbCo _{1.5} (H ₂ O)[B ₂ P ₃ O ₁₂ (OH)] Trimeric units of CoO ₆ and CoO ₄ (H ₂ O) ₂ octahedra sharing edges interconnect with the borophosphate slabs in a framework that includes Rb ⁺ ions in open channels.	9.501(1) 12.272(2) 20.074(2) 2340.6(5)	<i>Pbca</i> 8 2.925	2.101 (M = Co ²⁺)	3.219 3.236 3.300 (A = Rb)	24
CsCo _{1.5} (H ₂ O)[B ₂ P ₃ O ₁₂ (OH)] Trimeric units of CoO ₆ and CoO ₄ (H ₂ O) ₂ octahedra sharing edges interconnect with the borophosphate slabs in a framework that includes Cs ⁺ ions in open channels.	9.5526(4) 12.3190(4) 20.1123(8) 2366.8(1)	<i>Pbca</i> 8 3.16	2.104 2.145 (M = Co ²⁺)	3.331 3.351 3.400 (A = Cs)	25
Rb _{1.15} (H ₂ O) _{0.4} Mn _{1.5} [B ₂ P ₃ O ₁₂ (O,OH)] ^a Borophosphate slabs and chains of MnO ₆ and MnO ₄ polyhedra sharing edges and vertices, form a framework with Rb ⁺ ions and water molecules in open channels	9.151(1) 12.257(1) 20.076(2) 2251.8(2)	<i>Pbna</i> 8 3.000	2.182 (M = Mn ²⁺ in octahedron) 2.092 (in tetrahedron)	3.018 3.107 2.954 (A = Rb, H ₂ O)	Our data
(NH ₄)(C ₄ H ₁₂ N ₂) _{0.5} (H ₂ O) _{0.5} Co[B ₂ P ₃ O ₁₂ (OH)] Mixed anionic framework built by a 3D borophosphate network and CoO ₆ octahedra with NH ₄ ⁺ ions, organic and water molecules in intersecting channels	14.207(3) 24.956(6) 5037.1(2)	<i>I41/a</i> 8 2.384	2.097 (M = Co ²⁺)	(A = NH ₄ , C ₄ H ₁₂ N ₂ , H ₂ O)	26

^a Crystal characteristics are given in a non-standard setting of the space group $D_{2h}^{14} = Pbcn$ for consistency of data. ^b One Cd–Cl distance is included in calculation.

Co-centered octahedra to form a 3D open framework. Well-ordered protonated ethylenediamine molecules are fixed within the channels by hydrogen bonds. Later on, a series of isotopic orthorhombic compounds (C₂H₁₀N₂)M²⁺[B₂P₃O₁₂(OH)] with M = Mg, Mn, Fe, Ni, Cu, and Zn was hydrothermally synthesized and studied using single-crystal X-ray diffraction (for the Mg phase) or by Rietveld-methods.²¹

The Cd borophosphate, (C₂H₁₀N₂)Cd[B₂P₃O₁₂(OH)] (Fig. 8a), crystallizes in the same structure type.²² All these isotopic compounds reveal different unit cell volumes that obviously depend on the size of the M²⁺ cation (Table 3). Interestingly, using DETA as a structure-directing amine during the synthesis in the CdCl₂–B₂O₃–H₃PO₄–H₂O system leads to the formation of the (C₄H₁₆N₃)[CdClB₂P₃O₁₂(OH)] phase built by two-



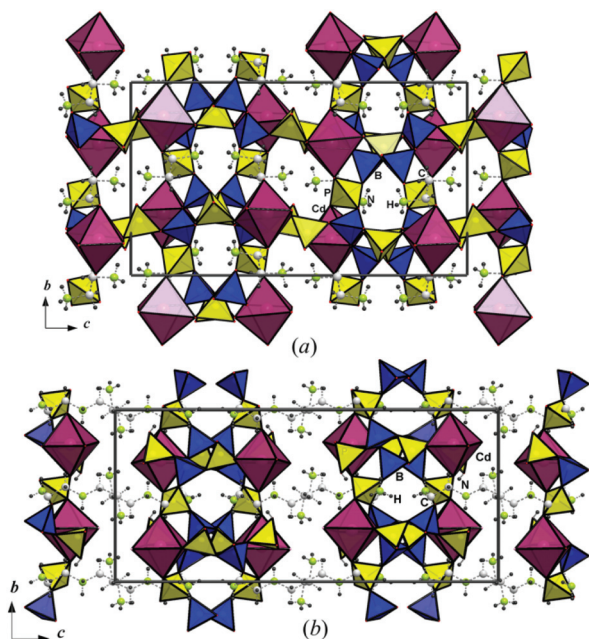


Fig. 8 Crystal structures of Cd borophosphates shown in the *yz* projections: $(\text{C}_2\text{H}_{10}\text{N}_2)\text{Cd}[\text{B}_2\text{P}_3\text{O}_{12}(\text{OH})]$ (a) and $(\text{C}_4\text{H}_{16}\text{N}_3)[\text{CdClB}_2\text{P}_3\text{O}_{12}(\text{OH})]$ (b).

dimensional inorganic fragments of the same borophosphate slabs with adjacent CdO_5Cl octahedra, separated by organic templates of diethylenetriamine (Fig. 8b).²² Accordingly, the *c* parameter of the $(\text{C}_4\text{H}_{16}\text{N}_3)[\text{CdClB}_2\text{P}_3\text{O}_{12}(\text{OH})]$ unit cell is changed significantly, and the inorganic structural fragments and organic DETA molecules alternate in the structure (Table 3).

Isostructural borophosphates, all having the same $D^{15}_{2h} = Pbc_a$ space group, may be obtained without organic templates. Two isotopic compounds, $[\text{K}_2(\text{H}_2\text{O})][\text{MB}_2\text{P}_3\text{O}_{12}(\text{OH})]$ [$\text{M} = \text{Co}$ or Ni], have been synthesized with K^+ ions instead of ethylenediamine as the organic template. They are constructed by the connection of tetrahedral layers and MO_6 octahedra, giving rise to a 3D framework with 8-ring channels aligned in the $[010]$ direction. The negative charge of the framework is compensated by the K^+ ions located in the 8-ring channels together with water molecules.²³

Two more compounds, $\text{A}^+_2\text{Co}_3(\text{H}_2\text{O})_2[\text{B}_4\text{P}_6\text{O}_{24}(\text{OH})_2]$ with alkaline ions, which play a directing role in the structure formation, were formed under hydrothermal conditions.^{24,25} Their isotopic crystal structures include trimeric units of CoO_6 and $\text{CoO}_4(\text{H}_2\text{O})_2$ octahedra sharing edges that further interconnect with the borophosphate slabs into a framework (Fig. 9). Large low-charged Rb^+ or Cs^+ ions occupy positions in open channels. Both orthorhombic phases are described by the same $D^{15}_{2h} = Pbc_a$ space group and similar unit cell parameters, which are naturally larger in the case of $\text{Cs}_2\text{Co}_3(\text{H}_2\text{O})_2[\text{B}_4\text{P}_6\text{O}_{24}(\text{OH})_2]$ (Table 3).

In contrast to the $(\text{C}_2\text{H}_{10}\text{N}_2)_2\text{M}_2^{2+}[\text{B}_4\text{P}_6\text{O}_{24}(\text{OH})_2]$ and $[\text{K}_2(\text{H}_2\text{O})][\text{MB}_2\text{P}_3\text{O}_{12}(\text{OH})]$ structures with isolated MO_6 octa-

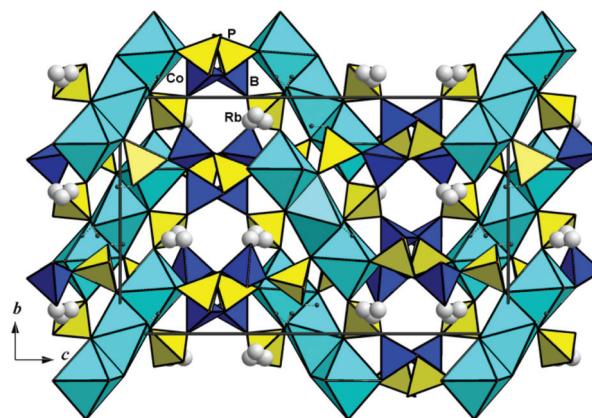


Fig. 9 The $\text{Rb}_2\text{Co}_3(\text{H}_2\text{O})_2[\text{B}_4\text{P}_6\text{O}_{24}(\text{OH})_2]$ crystal structure with three-dimensional borophosphate polyanions shown along the *a* axis.

hedra, or to the $\text{A}^+_2\text{Co}_3(\text{H}_2\text{O})_2[\text{B}_4\text{P}_6\text{O}_{24}(\text{OH})_2]$ structures with triplets of transition metal octahedra, the new compound $\text{Rb}_{2.3}(\text{H}_2\text{O})_{0.8}\text{Mn}_3[\text{B}_4\text{P}_6\text{O}_{24}(\text{O},\text{OH})_2]$ reveals Mn^{2+} cations with two distinct coordinations, the MnO_6 octahedra and MnO_4 tetrahedra that together form 1D chains. The observed structural transformation correlates with the change of the space group to $D^{14}_{2h} = Pbn_a$. It is worth noting that, despite having different crystal structures, three groups of compounds under discussion reveal nearly identical borophosphate slabs.

An exceptional crystal structure of $(\text{NH}_4)_2(\text{C}_4\text{H}_{12}\text{N}_2)(\text{H}_2\text{O})[\text{Co}_2\text{B}_4\text{P}_6\text{O}_{24}(\text{OH})_2]$ with the three-dimensional borophosphate polyanion formed by topologically equivalent $[\text{B}_2\text{P}_3\text{O}_{12}(\text{OH})]$ building blocks of three-membered rings of two borate and one phosphate tetrahedra features tetragonal symmetry (space group $I4_1/a$).²⁶ The CoO_6 octahedra are introduced into the borophosphate network to form a complex open framework with a three-dimensional intersecting channel system. Its voids are populated by ammonium and diprotonated piperazine ions and water molecules.

Magnetic properties

The dc-magnetic susceptibility χ in a wide temperature range follows the modified Curie–Weiss law with the temperature independent term

$$\chi = \chi_0 + \frac{C}{T - \theta'}$$

where $\chi_0 = -4 \times 10^{-4} \text{ emu mol}^{-1}$, the Curie constant $C = 13.2 \text{ emu K mol}^{-1}$, and the Weiss temperature $\theta' = -16 \text{ K}$ (Fig. S1†). The negative value of χ_0 originates from diamagnetic contributions of individual ions. The absolute value of this contribution is in quite good agreement with the sum of Pascal's constants yielding $-0.427 \times 10^{-3} \text{ emu mol}^{-1}$.²⁷ The Curie constant corresponds to the value of $8C = ng^2S(S+1) = 13.125 \text{ emu K mol}^{-1}$ expected for $n = 3 \text{ Mn}^{2+}$ ions in the chemical formula with the *g*-factor $g = 2$ and spin $S = 5/2$. The negative value of the Weiss temperature indicates the predominance of anti-ferromagnetic exchange interactions. At low temperatures,



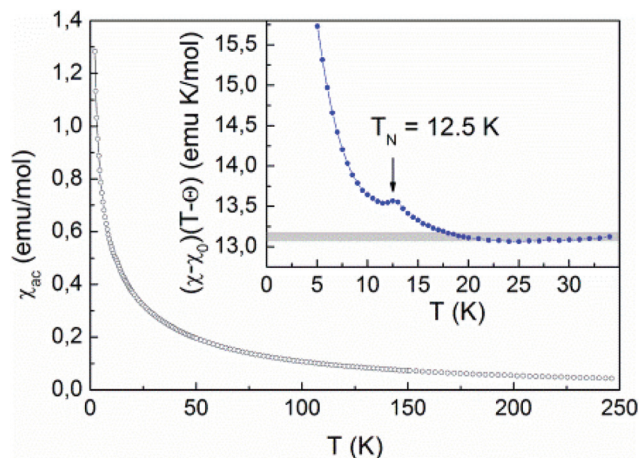


Fig. 10 The temperature dependence of the ac-magnetic susceptibility in $\text{Rb}_{2.3}(\text{H}_2\text{O})_{0.8}\text{Mn}_3[\text{B}_4\text{P}_6\text{O}_{24}(\text{O},\text{OH})_2]$. Inset: The temperature dependence of the product $(\chi - \chi_0)(T - \theta)$, the straight line represents the Curie constant at high temperatures.

experimental data deviate from the Curie–Weiss behavior toward larger values of the magnetic susceptibility.

The ac-magnetic susceptibility is in good agreement with the dc-data and reveals weak anomaly at $T_N = 12.5$ K, as shown in Fig. 10. This anomaly may signal long-range magnetic ordering in the system. In contrast to conventional antiferromagnets, the magnetic susceptibility increases below the transition and displays a paramagnetic-like behavior at low temperatures. Further evidence of the magnetic transition is provided by the specific heat measurements shown in Fig. 11. A rather smeared anomaly is seen at $T_N = 12.5$ K.

The field dependence of the magnetization is shown in Fig. 12. At 2.5 K, magnetization approaches the saturation value of $15\mu_B/\text{f.u.}$ around 27 T suggesting that a rather high magnetic field is required to overcome antiferromagnetic interactions between the Mn^{2+} spins. Additionally, deviations from linear behavior are seen around 4 T.

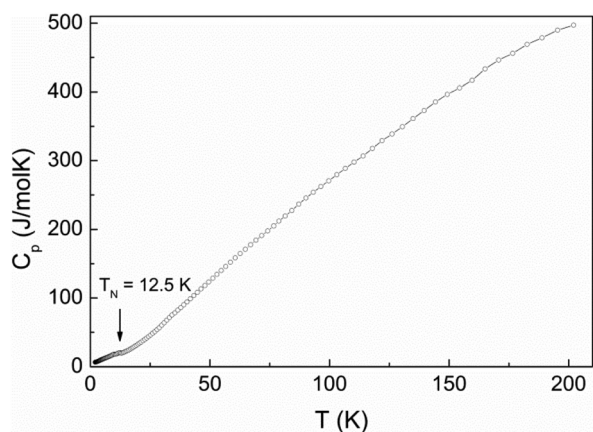


Fig. 11 The temperature dependence of specific heat C_p in $\text{Rb}_{2.3}(\text{H}_2\text{O})_{0.8}\text{Mn}_3[\text{B}_4\text{P}_6\text{O}_{24}(\text{O},\text{OH})_2]$.

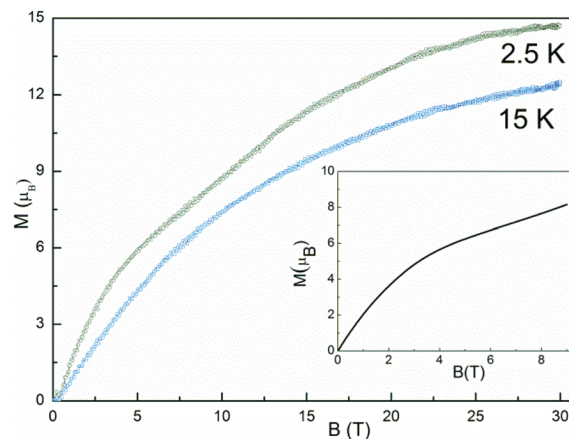


Fig. 12 The field dependences of magnetization M in $\text{Rb}_{2.3}(\text{H}_2\text{O})_{0.8}\text{Mn}_3[\text{B}_4\text{P}_6\text{O}_{24}(\text{O},\text{OH})_2]$ taken in a pulsed magnetic field. Inset: The field dependence of magnetization taken in a static magnetic field at 2 K.

Magnetic model

Individual magnetic couplings in $\text{Rb}_{2.3}(\text{H}_2\text{O})_{0.8}\text{Mn}_3[\text{B}_4\text{P}_6\text{O}_{24}(\text{O},\text{OH})_2]$ were obtained from total energies of collinear spin configurations calculated using the projected augmented wave formalism implemented in the VASP code.²⁸ For density-functional theory (DFT) band-structure calculations, the Perdew–Burke–Ernzerhof flavor of the exchange–correlation potential²⁹ was chosen. Strong correlations in the Mn 3d shell were taken into account of the mean-field DFT+ U level³⁰ with the on-site Coulomb repulsion $U = 7$ eV and Hund's exchange $J = 1$ eV.³¹ Each magnetic coupling was derived from the total energies of four collinear spin configurations, as further explained in ref. 32. We used the experimental crystal structure that was modified as follows: (i) the Rb1 position was 100% occupied, while the sparsely occupied Rb2 and Rb3 positions were excluded; (ii) the O14 and O15 positions (disordered water molecules) were excluded too. These modifications change the overall composition to $\text{Rb}_2\text{Mn}_3[\text{B}_4\text{P}_6(\text{OH})_2\text{O}_{24}]$ without affecting the charge distribution and valence state of Mn. Since neither Rb nor water molecules are directly bonded to the Mn atoms, their effect on the magnetic couplings should be minor.

Magnetic couplings J_i are calculated for pairs of spin-5/2 Mn^{2+} ions. Positive couplings are antiferromagnetic. In $\text{Rb}_{2.3}(\text{H}_2\text{O})_{0.8}\text{Mn}_3[\text{B}_4\text{P}_6\text{O}_{24}(\text{O},\text{OH})_2]$, three nearest-neighbor couplings are $J_1 = 0.14$ K (3.478 Å, Mn1–Mn1), $J_2 = 3.4$ K (3.632 Å, Mn1–Mn2), and $J_3 = -0.01$ K (4.065 Å, Mn1–Mn2), where numbers in brackets stand for Mn–Mn distances (Fig. 13). The couplings beyond the nearest neighbors are below 0.02 K.

The difference between the nearest-neighbor couplings J_1 and J_2 is rooted in the different Mn–O–Mn angles, 103.74° and 115.59° , respectively. According to Goodenough–Kanamori–Anderson rules, larger Mn–O–Mn angles favor antiferromagnetic couplings, hence $J_2 > J_1$. Despite its relatively short



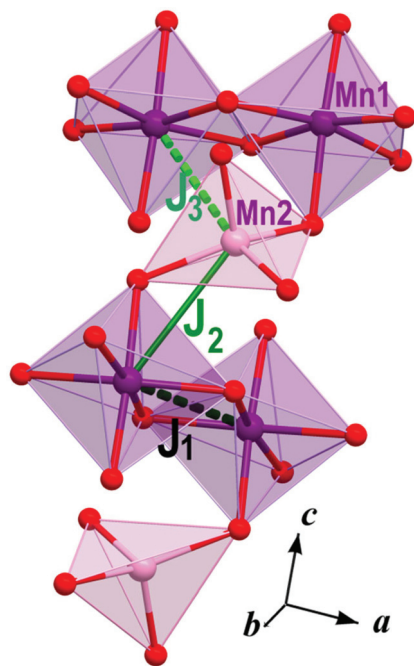


Fig. 13 The exchange paths for various magnetic interactions.

Mn–Mn distance, the coupling J_3 is between the Mn1O_6 octahedron and Mn2O_4 tetrahedron that are not directly connected to each other. Therefore, no Mn–O–Mn superexchange pathway exists, and the coupling J_3 remains weak.

The coupling J_2 builds Mn1–Mn2–Mn1 trimers. The magnetic susceptibility of spin-5/2 trimers obtained from quantum Monte-Carlo simulations with $J = 3.2$ K, $g = 1.98$, and $\chi_0 = -4 \times 10^{-4}$ emu mol $^{-1}$ perfectly reproduces experimental data down to 20 K (Fig. S1†). This exchange coupling is in excellent agreement with the calculated $J_2 = 3.4$ K. The trimer model explains the increase in the susceptibility toward lower temperatures. Indeed, at low temperatures an individual trimer adopts the spin-5/2 state and behaves as a paramagnetic entity with the diverging susceptibility. Below 20 K, the magnetic transition at T_N and ensuing deviations from the spin-trimer behavior are likely due to antiferromagnetic couplings between the trimers. However, these couplings are too weak for a reliable quantitative analysis.

For a spin-5/2 trimer with $J = 3.2$ K one expects saturation at $H_s \sim 20$ T. Experimentally, the saturation feature is very broad, and the saturation field cannot be determined with sufficient accuracy. Nevertheless, at 2.5 K and 20 T the magnetization reaches around 90% of the saturated value, which means that our estimate of J is in reasonable agreement with the magnetization data.

Conclusions

$\text{Rb}_{2.3}(\text{H}_2\text{O})_{0.8}\text{Mn}_3[\text{B}_4\text{P}_6\text{O}_{24}(\text{O},\text{OH})_2]$ is a new borophosphate compound that reveals an original crystal structure. In contrast

to other borophosphates with similar structural units, it shows an interesting combination of the magnetic high-spin Mn^{2+} ions in both octahedral and tetrahedral coordinations. The ensuing magnetic interactions give rise to antiferromagnetic spin trimers that manifest themselves in the paramagnetic-like behavior, with the magnetic susceptibility increasing upon cooling. Weak interactions between these trimers induce a magnetic transition (presumably, antiferromagnetic ordering) around 12.5 K.

Acknowledgements

This work was supported in part by the Ministry of Education and Science of the Russian Federation in the framework of the Increase Competitiveness Program of NUST “MISIS” Grants No. K2-2016-066 and K4-2015-020, by Act 211 of the Government of Russian Federation, agreement No. 02. A03.21.0006, and by the Russian Foundation for Basic Research Grants No. 15-05-06742, 16-02-00021 and 17-02-00211. AT acknowledges financial support by the Federal Ministry for Education and Research through the Sofja Kovalevskaya Award of the Alexander von Humboldt Foundation.

Notes and references

- B. Ewald, Y.-X. Huang and R. Kniep, *Z. Anorg. Allg. Chem.*, 2007, **633**, 1517.
- O. Yakubovich, I. Steele, W. Massa and O. Dimitrova, *Z. Kristallogr.*, 2013, **228**, 509.
- H. Li and A.-V. Mudring, *Cryst. Growth Des.*, 2016, **16**, 2441.
- H. Yaghoobnejad, P. Stanly, K. Ghosh and A. Choudhury, *Chem. Mater.*, 2015, **27**, 7058.
- M. Mouyane, J. C. Jumas, J. Olivier-Fourcade, S. Cassignon, Ch. Jordy and P. E. Lippens, *J. Solid State Chem.*, 2016, **233**, 52.
- J. A. L. Da Silva and N. G. J. Holm, *Colloid Interface Sci.*, 2014, **431**, 250.
- T. Su, H. Xing, J. Xu, J. Yu and R. Xu, *Inorg. Chem.*, 2011, **50**, 1073.
- W. Zhang, W. Cheng, H. Zhang, L. Geng, Y. Li, Ch. Lin and Zh. He, *Inorg. Chem.*, 2010, **49**, 2550.
- M. Yang, P. Yan, F. Xu, J. Ma and U. Welz-Biermann, *Microporous Mesoporous Mater.*, 2012, **147**, 73.
- G. Wang, M. Valldor, Ch. Lorbeer and A.-V. Mudring, *Eur. J. Inorg. Chem.*, 2012, **18**, 3032.
- W. Yang, J. Li, T. Na, J. Xu, L. Wang, J. Yu and R. Xu, *Dalton Trans.*, 2011, **40**, 2549.
- CrysAlisPro*, Oxford diffraction Ltd, 2014, Version 1.171.37.31 (release 14-01-2014 CrysAlis171.NET).
- L. J. Farrugia, *J. Appl. Crystallogr.*, 2012, **45**, 849.
- International Tables for Crystallography*, ed. E. Prince, Kluwer, Dordrecht, 3rd edn, 2004, Tables 4.2.6.8 and 6.1.14.



- 15 G. M. Sheldrick, *Acta Crystallogr., Sect. C: Cryst. Struct. Commun.*, 2015, **71**, 3.
- 16 I. D. Brown and D. Altermatt, *Acta Crystallogr., Sect. B: Struct. Sci.*, 1985, **41**, 244.
- 17 I. D. Brown, *Chem. Rev.*, 2009, **109**, 6858.
- 18 H. B. Yahia, E. Gaudin and J. Darriet, *J. Alloys Compd.*, 2007, **442**, 74.
- 19 M. Luján, F. Kubel and H. Schmid, *Z. Naturforsch., B: J. Chem. Sci.*, 1995, **50**, 1210.
- 20 S. C. Sevov, *Angew. Chem., Int. Ed. Engl.*, 1996, **35**, 2630.
- 21 R. Kniep and G. Schäfer, *Z. Anorg. Allg. Chem.*, 2000, **626**, 141.
- 22 W. Liu, M. Ge, X. Yang, H. Chen, M. Li and J. Zhao, *Inorg. Chem.*, 2004, **43**, 3910.
- 23 D. Zhang, Y. Feng, Y. Lin, Y. Zhang, G. Li and H. Yuan, *Dalton Trans.*, 2015, **44**, 17100.
- 24 H. Engelhardt, W. Schnelle and R. Kniep, *Z. Anorg. Allg. Chem.*, 2000, **626**, 1380.
- 25 P. W. Menezes, S. Hoffmann, Yu. Prots and R. Kniep, *Z. Kristallogr. – New Cryst. Struct.*, 2009, **224**, 1.
- 26 W. Liu, X.-Q. Guo, G. Su, L.-X. Cao, Y.-G. Wang and J.-R. Duan, *J. Solid State Chem.*, 2011, **184**, 2538.
- 27 G. A. Bain and J. F. Berry, *J. Chem. Educ.*, 2008, **85**, 532.
- 28 G. Kresse and J. Furthmüller, *Mater. Sci.*, 1996, **6**, 15; G. Kresse and J. Furthmüller, *Phys. Rev. B: Condens. Matter*, 1996, **54**, 11169.
- 29 J. P. Perdew, K. Burke and M. Ernzerhof, *Phys. Rev. Lett.*, 1996, **77**, 3865.
- 30 A. I. Liechtenstein, V. I. Anisimov and J. Zaane, *Phys. Rev. B: Condens. Matter*, 1995, **52**, R5467.
- 31 R. Nath, K. M. Ranjith, B. Roy, D. C. Johnston, Y. Furukawa and A. A. Tsirlin, *Phys. Rev. B: Condens. Matter*, 2014, **90**, 024431.
- 32 H. Xiang, C. Lee, H.-J. Koo, X. Gong and M.-H. Whangbo, *Dalton Trans.*, 2013, **42**, 823.

